ELM-free H-mode phase and decoupling of peeling–ballooning stability boundary in the MAST Upgrade tokamak

OPEN ACCESS
IOP Publishing
Plasma Physics and Controlled Fusion
Plasma Phys. Control. Fusion **66** (2024) 125011 (12pp)
https://doi.org/10.1088/1361-6587/ad877c

ELM-free H-mode phase and decoupling of peeling–ballooning stability boundary in the MAST Upgrade tokamak

K Imada[1,2,*], T H Osborne[1], S Saarelma[3], A Kirk[3], S Blackmore[3], M Knolker[1], R Scannell[3], P B Snyder[4], C Vincent[3], H R Wilson[4] and the MAST Upgrade Team[3]

[1] General Atomics, San Diego, CA 92186-5608, United States of America
[2] York Plasma Institute, School of Physics, Electronics and Engineering, University of York, Heslington, York YO10 5DD, United Kingdom
[3] UKAEA, Abingdon, Oxon, OX14 3DB, United Kingdom
[4] Oak Ridge National Laboratory, Oak Ridge, TN 37831, United States of America

E-mail: koki.imada@york.ac.uk

Received 14 May 2024, revised 2 September 2024
Accepted for publication 16 October 2024
Published 4 November 2024

Abstract

A linear magnetohydrodynamic (MHD) peeling–ballooning stability analysis of the edge-localized mode (ELM)-free phase of a MAST Upgrade (MAST-U) H-mode plasma is presented. In contrast to other similar discharges, #47018 is found to have a significantly higher and wider pedestal during its ELM-free H-mode phase that lasts for approximately 80 ms; this is made possible by the reduced core MHD mode activity on the $q = 2$ surface. During this period, there is sustained decoupling of peeling and ballooning branches of the stability boundary on J–α space, opening an access channel to the second stability regime with higher peaks in pedestal current density $J_{\mathrm{N,ped}}$ and pressure gradient (α). Such decoupling of the stability boundary has not previously been observed in MAST-U H-modes, and if such a condition can be readily reproduced, it opens a wide range of opportunities for MAST-U to explore low-collisionality peeling-limited pedestal regimes as well as advanced scenarios such as quiescent H-modes that are relevant to future reactors such as STEP and ITER.

Keywords: pedestal stability, spherical tokamak, MAST Upgrade, ELMs

1. Introduction

In order to achieve conditions relevant for future tokamak fusion power plants, it is necessary to maximize the density and temperature of the plasma as well as the energy confinement time [1]. One way to achieve this is to operate the tokamak plasma in high-confinement (or H-) mode [2], which is characterized by the formation of a pedestal with a steep radial pressure gradient, elevating the core plasma profile. However, the pedestal height and gradient are often limited by the onset of peeling–ballooning instabilities, resulting in periodic outbursts of plasma filaments known as edge-localized modes (ELMs) [3–6]. With each outburst, a fraction of the confined particles and heat are ejected beyond the last closed flux surface and eventually deposited onto the vessel walls. ELMs can be categorized into a number of different types, depending on the physics behind the outburst mechanism as well as the size and frequency of the outbursts. Type I ELMs are typically the largest, often with up to 25% of the pedestal thermal energy ejected in a single event; if left uncontrolled, these can cause serious damage to plasma-facing components. Therefore, while the improved core confinement in a standard H-mode is beneficial, future power plants will have to operate in an ELM-free regime.

* Author to whom any correspondence should be addressed.

This paper is concerned with the pedestal stability analysis of an ELM-free period observed in MAST Upgrade (MAST-U) H-mode discharges. MAST-U is a recently upgraded spherical tokamak operated by UKAEA. Previous analysis [7] has shown that, contrary to its predecessor, MAST, whose type I ELMy H-mode discharges were almost always ballooning limited [8–10], the pedestal stability of MAST-U plasmas have mixed characteristics: although ultimately limited by the ballooning branch of the stability boundary in most cases, the pedestal is shown to be close to the peeling branch as well, sitting in a narrow channel of stability resulting from reduced coupling between the peeling and ballooning modes. One of the contributing factors is that MAST-U is a radically different shape from its predecessor, with significantly higher elongation and larger squareness for comparable triangularity. Previously, a number of low-collisionality peeling-limited pedestal H-mode attempts were made. Although they were successful in so far as they eliminated the onset of ELMs, a steep rise in pedestal density resulted in large density collapse events, often dropping out of the H-mode phase. However, one discharge from our recent experiments, #47018, exhibited a considerably longer ELM-free period in the early part of the H-mode phase. As discussed in detail later, our pedestal stability analysis shows that there was a decoupling of the peeling and ballooning branches of the pedestal stability boundary, with the plasma located very close to the peeling branch.

In this paper, this discharge will be examined in detail due to its interesting pedestal behavior in terms of its peeling–ballooning stability. In section 2, an introduction to pedestal stability physics is given, followed by an overview of the experimental data and measurements in section 3. In section 4, the results of the pedestal stability analysis are presented, including a comparison with other similar H-mode discharges in MAST-U. Detailed discussions on the results and overall conclusions are presented in sections 5 and 6, respectively.

2. Background to pedestal stability analysis

The magnetohydrodynamic (MHD) stability of the pedestal region can be described in terms of the peeling–ballooning theory [11], according to which the two key plasma parameters that define the pedestal stability limit are the normalized pedestal current density, $J_{\mathrm{N,ped}}$, and normalized pedestal pressure gradient, $\alpha_{(\mathrm{ped})}$. These two normalized quantities are defined as

$$J_{\mathrm{N}} = \frac{J_{\mathrm{PB}}\left(\psi\right) + J_{\mathrm{PB}}\left(\psi_{\mathrm{separatrix}}\right)}{2I\left(\psi\right)/A\left(\psi\right)} \tag{1}$$

$$\alpha = \frac{\mu_0}{2\pi^2}\frac{\partial V}{\partial \psi}\left(\frac{V}{2\pi^2 R}\right)^{1/2}\frac{\mathrm{d}p}{\mathrm{d}\psi}, \tag{2}$$

where $J_{\mathrm{PB}} = (RB_T/R_0)\langle J_{\parallel}/B\rangle$ is a combination of flux surface-averaged (denoted by $\langle\ldots\rangle$) parallel current and Pfirsch–Schlüter current densities, ψ is the poloidal magnetic flux, $I(\psi)$ is the toroidal current within a flux surface of cross-sectional area $A(\psi)$, R_0 is the major radius of the geometric center, V is the volume enclosed by a flux surface at ψ and $\mathrm{d}p/\mathrm{d}\psi$ is the pressure gradient. In a typical H-mode, α is peaked in the pedestal region because of the steep radial pressure gradient, which also leads to a peak in J_{N} because of the increased bootstrap current that is proportional to the pressure gradient (provided the plasma collisionality ν_* is sufficiently low). In a simplified picture, exceeding the stability limit on α triggers the growth of near-ideal ballooning modes [12], with typically high toroidal mode numbers n. These ideal ballooning modes can be stabilized by increasing the peak in pedestal current density, $J_{\mathrm{N,ped}}$. On the other hand, exceeding the limit on $J_{\mathrm{N,ped}}$ at lower α results in peeling modes, with typically low toroidal mode numbers [13]. In reality, the complex interplay between the peeling and ballooning modes means it is rare to encounter pure ballooning or pure peeling modes. Moreover, the coupling between them sets upper limits on the maximum values of $J_{\mathrm{N,ped}}$ and α that are attainable without triggering an ELM, thus defining a stability boundary on the J–α space. Quantitative analysis of pedestal stability requires the inclusion of non-local effects [4], which determine the degree of peeling–ballooning coupling to the leading order, as well as the global Shafranov shift [14] and poloidal cross-sectional shape defined in terms of elongation κ, triangularity δ [15] and squareness ζ [7, 16]. (There are other contributing factors such as scrape-off layer and divertor configurations, which are beyond the scope of the present analysis.)

One goal of pedestal stability research is to find optimum configurations of plasma parameters to minimize or break the coupling between peeling and ballooning modes, to open an access channel to the second stability region [17] with significantly higher $J_{\mathrm{N,ped}}$ and α. For example, increasing plasma elongation generally increases ballooning stability (and also the peeling stability to a lesser extent), while higher triangularity has a greater impact on stabilizing peeling modes. Thus, optimized shaping can help to decouple the peeling and ballooning branches at higher α values. In addition, electron pedestal collisionality $\nu_{*\mathrm{e,ped}}$ plays a role in setting the ratio of peak $J_{\mathrm{N,ped}}$ and α values: lower collisionality means lower resistivity, which can result in higher $J_{\mathrm{N,ped}}$ values for given α. In terms of the operational window, this is desirable because the pedestal can evolve while keeping a distance from the ballooning stability limit, thus avoiding type I ELMs. During an inter-ELM period, an accumulation of pedestal density increases collisionality, thus naturally limiting the increase in $J_{\mathrm{N,ped}}$ at given α (desirably before the peeling stability boundary is crossed). Therefore, one path to accessing the second stability region with significantly elevated $J_{\mathrm{N,ped}}$ and α is to operate with a peeling-limited, low pedestal collisionality configuration in a strongly shaped plasma with high elongation and triangularity. This would enable us to explore more advanced ELM-free regimes, such as quiescent-H (QH) modes [18] and I-modes [19], eventually super-H modes with adequate heating power.

The focus of this paper is a steady-state ELM-free period observed in the aforementioned MAST-U H-mode discharge

#47018 (lasting over 80 ms, compared with a typical inter-ELM period of 20–40 ms under similar conditions). This period was accompanied by a notably higher pedestal top electron temperature, in excess of 300 eV compared with the typical 200–250 eV. Our MHD stability analysis reveals stark contrasts between #47018 and similar discharges, as follows. The other discharges, #46977 and #47020, were more 'ballooning limited' in the typical MAST-U H-mode characteristic, with a narrow stable region extending between the peeling and ballooning branches of the stability boundary. On the other hand, for #47018 there was a clear decoupling of the stability boundary branches, with the pedestal able to access significantly higher values of $J_{\mathrm{N,ped}}$ and α. As discussed in detail later, a likely explanation involves the slightly different evolution of the safety factor (q) profiles, the absence of core MHD instability (a steady-state tearing mode) in #47018, which is prevalent in MAST-U H-modes shortly after the L–H transition, as well as different durations of the type III ELMy period following the L–H transition. It is believed that these factors have contributed to the particularly higher pedestal top temperature of #47018, allowing it to evolve away from the ideal ballooning stability limit but instead towards the peeling limit without triggering ELMs. As discussed in detail later, whether the pedestal during this ELM-free period is purely peeling-limited or not remains inconclusive because, while the mode number of #47018 is considerably lower than the others, there are no clear distinctions in the radial and poloidal mode structures when compared with the other discharges. However, if this ELM-free phase is made more readily accessible, it will open a significant opportunity for MAST-U to explore the peeling-limited pedestal regime, as well as advanced H-mode scenarios such as QH modes, which have not been achieved in spherical tokamaks to date. These will be critical for compact pilot fusion reactors such as STEP.

Pedestal stability analysis is carried out as follows, in the same way as outlined in our previous work [7]. Firstly, the OMFIT [20, 21] kineticEFITtime module is used to create radial plasma profiles using the following diagnostic measurements: Thomson scattering (TS) for electron density and temperature; carbon impurity (12C6) charge exchange data for ion temperature and toroidal rotation; the motional Stark effect (MSE) for magnetic field pitch, together with magnetic EFIT [22] data. Profiles are created by taking the average of diagnostic measurements in the inter-ELM periods (blue shades in figure 1), typically over the range between 20 and 30 ms. Since direct measurements of impurity species density are not available for MAST-U, an effective charge of $Z_{\mathrm{eff}} = 1.8$ is assumed, following standard procedures for MAST-U and its predecessor MAST [7, 9, 10]. The fitted profile lacks a contribution from fast ions, which is obtained by the transport code TRANSP [23, 24]. A MHD equilibrium reconstruction is then carried out by EFIT++ (a rewrite of the original EFIT) [25]. A goal of our pedestal stability analysis is to determine the location of the peeling–ballooning stability boundary relative to the experimental point on the J–α diagram. Therefore, in the second step the VARYPED code [26, 27] is used to generate a set of model fixed-boundary equilibria with varying $J_{\mathrm{N,ped}}$ and α. In the final step, the set of modeled equilibria is analyzed for peeling–ballooning stability using ELITE [4, 28], from which the stability boundary on the J–α space is determined. In the present analysis, the stability boundary is defined as the mode growth rate γ exceeding approximately 5% of the Alfvén frequency, ω_A ($\gamma/\omega_A = 0.04 \sim 0.06$ depending on discharges)[5], which is found to be consistent with most MAST-U type I ELMy H-mode cases.

3. Experimental setup and measurements

3.1. Machine and discharge setup

Three MAST-U H-mode discharges are compared in our present analysis. They are of standard double-null divertor configuration, with 3.15–3.25 MW of heating power from two neutral beam injection systems, plasma current (I_p) of 750 kA and a toroidal magnetic field strength (B_T) of 0.6 T. The first discharge, #46977, is the reference for the other two, #47018 and #47020. In the time frames analyzed in this paper, the three discharges are identical to each other in setup[6] (see table 1 and figure 2). The initial plasma current ramp-up phases are virtually identical for all three (following the L–H transition at ∼150 ms is the type III ELM period, which is marginally shorter for #47018). A crucial difference in the evolution between #47018 and the other two discharges can be seen in the magnetic perturbation spectra (figure 3). As toroidal Alfvén eigenmodes (TAEs) cascade down from >100 kHz, in #46977 and #47020 a prominent 10 kHz signal is clearly visible from ∼210 ms, the timing of which coincides with q_0 dipping below 2 (see also figure 1), where q_0 is the safety factor on the magnetic axis. This mode is usually attributed to a core MHD mode (usually a steady-state tearing mode on the $q = 2$ surface) [29, 30] and is commonly observed in MAST-U ELMy H-modes. On the other hand, no such trace of MHD modes is visible for #47018 in the early part of the H-mode phase, until the TAEs have slowed down and disappeared after 350 ms (also the case for #46977 and #47020). It is worth noting that q_0 does not drop below 2 until about 280 ms, considerably later than the other two discharges, which is likely to have consequences for the onset of the MHD modes, as discussed later.

3.2. Profile reconstruction and equilibrium analysis

Figure 4 shows the fitted plasma profiles for discharges #46977, #47018 and #47020, all in the 320 ms time frame. Because these three discharges have an identical setup until

[5] The variation is in part due to the differences in ion density profile, which results in differences in Alfvén frequency.

[6] The only difference in the discharge settings between them is the application of X-point radial position shift of 2.5 cm to increase triangularity from 350 ms to 450 ms, with the effect on X-point position taking place from ∼380 ms, which is after the time frame analyzed in this paper.

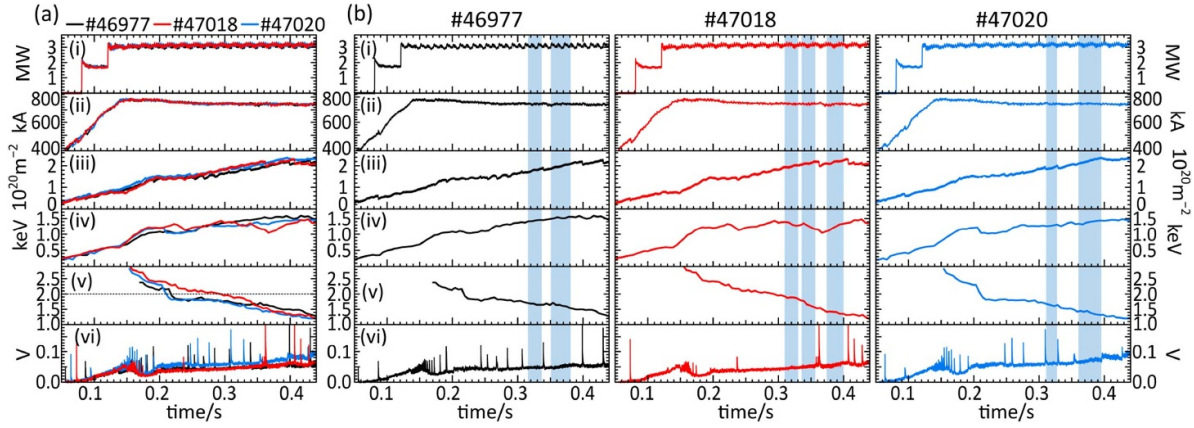

Figure 1. Plasma discharge trajectories for discharges #46977, #47018 and #47020 ((a) overlaid, (b) individual discharges): (i) combined heating power from two neutral beam injection systems, (ii) plasma current, (iii) line-integrated electron density, (iv) core electron temperature, (v) safety factor at magnetic axis, q_0 ($q_0 = 2$ shown with the dotted line), (vi) Dα emission illustrating ELM events. Blue shading indicates the time slices used for the present analysis. The trajectory for MAST #30422 is presented in reference [7].

Table 1. List of parameters for discharges #46977, #47018 and #47020. Parameters from MAST discharge #30422 are also shown for comparison. κ, δ and ζ are plasma elongation, triangularity and squareness respectively (up–down averaged), $\beta_N = \beta a B_T / I_p$, where β is the plasma beta and a is the minor radius, $\nu_{*\mathrm{e,ped}}$ is the electron pedestal collisionality and $T_{\mathrm{e,ped}}$ and $p_{,\mathrm{ped}}$ are electron temperature and total plasma pressure at the pedestal top.

Discharge #	30422	46977	47018	47020
Time label (ms)	326	320365	320346386	320377
κ	1.55	2.14–2.18	2.15–2.18	2.08–2.14
δ	0.45	0.45–0.49	0.42–0.48	0.45–0.54
ζ	0.21	0.37–0.38	0.38	0.37–0.38
β_{N}	2.4	1.8	1.9–2.3	2.0
$\nu_{*\mathrm{e,ped}}$	2.1	1.4	1.0–1.3	1.4
$T_{\mathrm{e,ped}}$ (keV)	0.16	0.24–0.28	0.31–0.35	0.27–0.29
$p_{,\mathrm{ped}}$ (kPa)	1.3	2.1–2.7	4.5–4.9	3.4–3.6
$J_{\mathrm{N,ped}}$	0.45	0.79–0.96	1.0–1.4	0.75–1.3
α	3.2	10.8–12.0	11.4–17.3	8.7–12.6

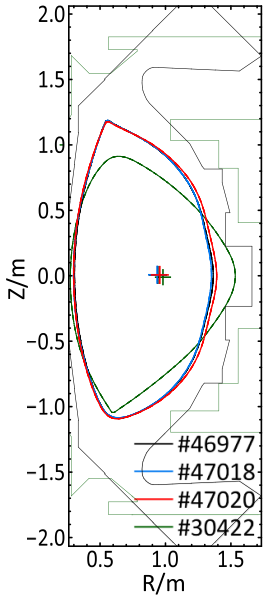

Figure 2. Comparison of poloidal cross section shape between the trio of MAST-U discharges #46977, #47018 and #47020 and MAST discharge #30422. The three MAST-U discharges are identical in setup, up to approximately 380 ms.

350 ms, the reconstructed equilibrium profiles are broadly similar except for two key differences. The first is that the pedestal density for #47018 is notably higher than the other two, most likely due to the long ELM-free period resulting in particle accumulation. The second is in the electron temperature profile: again, most likely because of the long ELM-free period, T_{e} is generally higher for #47018 throughout the radial profile by up to 100 eV ($\sim$ 30 eV higher at the pedestal top).

Figure 5 shows the reconstructed MHD equilibrium profile from the fixed-boundary EFIT run on the combination of the fitted profiles from the OMFIT kineticEFITtime module and fast ion data from TRANSP. The current density profile is a combination of the induced toroidal current, those calculated from magnetic measurements and the bootstrap current density profile calculated using the Sauter model [31, 32]. For #47018, the combination of broader pedestal density accumulation and higher pedestal top temperature gives a significantly higher and wider pedestal, which is also clear from the locations of the peak values of $J_{\mathrm{N,EFIT}}$ and α. Importantly, this leads to a subtle difference in the pedestal q-profiles: whereas #46977 and #47020 have more smoothly varying q-profiles across the pedestal region (with a small dip in the S-profile at the peak in $J_{\mathrm{N,EFIT}}$), there is a much clearer flattening in the q-profile of #47018 (with a significantly greater drop in S). One explanation is that because of high pedestal top temperature, the pedestal collisionality is notably lower for #47018 (see table 1), which helps to raise the peak pedestal current density, $J_{\mathrm{N,ped}}$, locally reducing the q-value there (higher poloidal magnetic field component). This partial flattening in the q-profile contributes to the exceedingly high peak in α (through

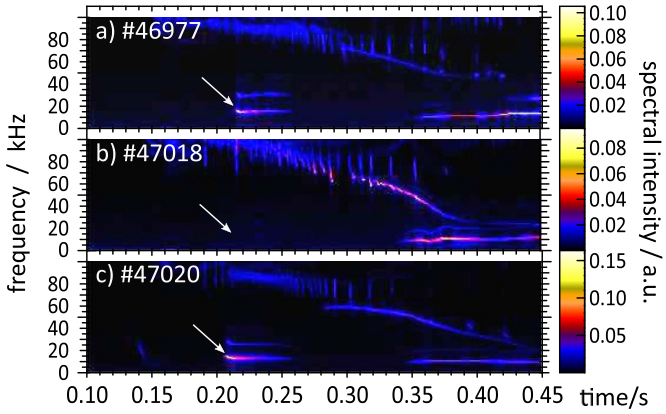

Figure 3. Frequency spectra of plasma perturbations for discharges (a) #46977, (b) #47018 and (c) #47020. The mode typically present at around 10 kHz is seen in #46977 and #47020, together with respective second harmonics at 20 kHz, but they are absent in #47018. Note the different color scaling for the three discharges; the cascading modes at higher frequency and 10 kHz mode signals from 350 ms onward are more or less comparable in signal strength for the three discharges.

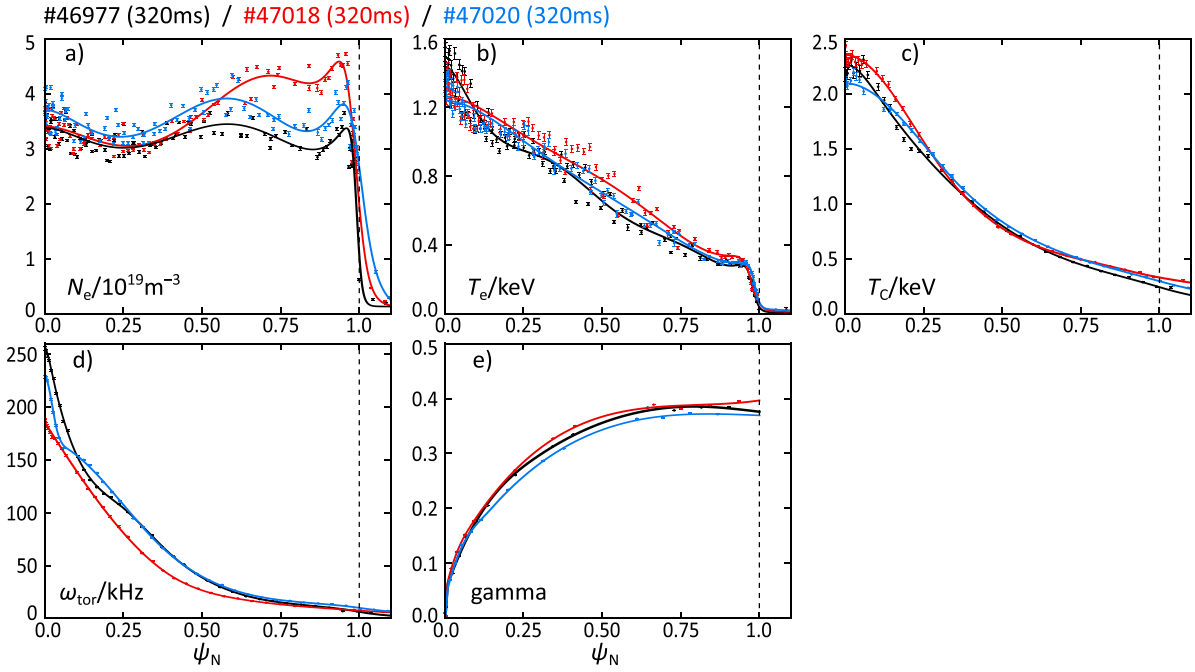

Figure 4. Fitted plasma profiles for #46977, #47018 and #47020, all at 320 ms: (a) electron density (N_e); (b) electron temperature (T_e); (c) carbon impurity temperature (T_C); (d) toroidal rotation frequency (ω_{tor}); (e) magnetic pitch ('gamma') calculated from the MSE data.

$\partial V/\partial\psi$ in equation (2), in addition to the already steep pressure gradient) for #47018, which is likely to contribute to the significant differences in the pedestal stability diagram, as discussed below.

4. Pedestal stability analysis with ELITE

4.1. General comparison

Figure 6 shows the results of ELITE pedestal stability calculations for the three discharges, all in the 320 ms time frame, with the distribution of the most unstable toroidal mode numbers (gray–white) and the location of the stability boundary (yellow solid lines). The stability boundary branch at higher $J_{N,ped}$ and lower α values along lower toroidal mode numbers corresponds to the peeling limit, whereas the branch that limits the α values at lower $J_{N,ped}$ corresponds to the ballooning stability boundary. In general, where the two branches meet at higher $J_{N,ped}$ and α values is where the mixture of peeling–ballooning modes can be triggered should the pedestal cross the stability boundary into the unstable region [4, 27, 33].

Both #46977 and #47020 exhibit the typical characteristics of MAST-U ELMy H-modes, with both the peeling and ballooning branches of the stability boundary present, joining at moderately high values of $J_{N,ped}$ and α. As discussed in

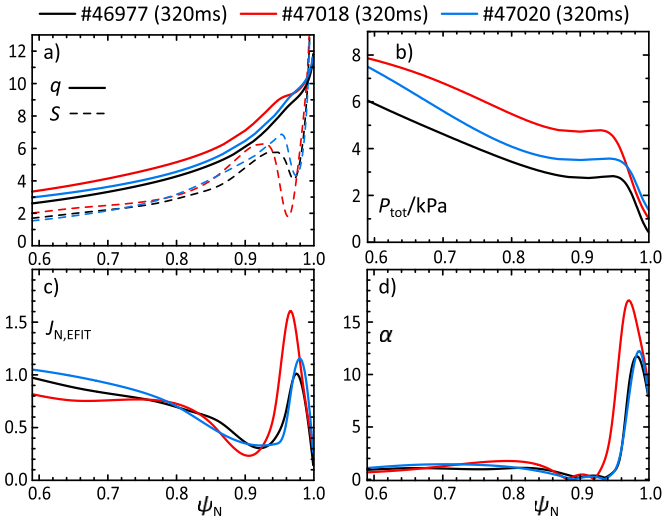

Figure 5. Comparison between discharges #46977, #47018 and #47020 of the EFIT results for: (a) the safety factor (q) and magnetic shear (S) profiles; (b) total plasma pressure (P_{tot}); (c) normalized current density, $J_{N,EFIT} = \langle J_T R_0/R\rangle/(\langle R_0/R\rangle J_{ave})$; (d) normalized pressure gradient (α), as functions of ψ_N. Here, J_T is the toroidal current density and J_{ave} is the current density averaged over the poloidal cross section at ψ_N.

[7], the extended region of stability between the two boundary branches is an indication of the weakened coupling between the peeling and ballooning modes. (Note that if a mode is triggered in this region by crossing the boundary, it is very likely the coupled peeling–ballooning mode rather than ideal high-n ballooning or pure peeling modes.) There are some differences between the two discharges, most notably in the toroidal mode numbers n. For #46977, n is in the range 30–40 around the experimental point (yellow cross), indicating that it is closer to an ideal ballooning-limited pedestal. On the other hand, for #47020 n is in the slightly lower range of 25–30 around the experimental point, although it is still comparable to other MAST-U ballooning-limited pedestals such as #45272. For both #46977 and #47020, the experimental points are away from the region of lower n (5–10) at lower α and moderate $J_{N,ped}$, where the pure peeling branch of the stability boundary is located. While the experimental points are within the extended region of stability, they are ultimately closer to the ballooning branch of the stability boundary and remain so at later time frames as well (see figure 7).

The stability diagram for #47018 in figure 6, on the other hand, is substantially different from the rest. There is still a well-defined peeling branch of the stability boundary (see also figure 8), but instead of joining the ballooning branch at finite $J_{N,ped}$ and α, it continues up beyond the calculation domain. The lower $J_{N,ped}$–α end still corresponds to the low-n peeling limit ($n = 5$ around the boundary), but there is mixture of intermediate mode numbers (15–25) in the vicinity of the experimental point, indicative of mixed peeling–ballooning modes that can be triggered, and some higher mode numbers in between. This wide variation in mode numbers suggests that there is no clear peak in the mode growth rate as a function of n, i.e. there is a wide range of modes that can be triggered.

There is a secondary stability boundary branch at lower values of $J_{N,ped}$ and α, which may be referred to as the 'ballooning' branch (contrasting with the 'peeling' branch described above). However, given the distribution of generally lower mode numbers in its vicinity, the actual high-n ideal ballooning boundary is likely to be located at lower values of $J_{N,ped}$ and α, just below the calculation domain. According to figure 8, the location of the upper 'peeling' branch varies very little with the mode growth threshold, γ/ω_A, which makes the stability boundary well-defined. However, the location of the lower 'ballooning' branch changes considerably with γ/ω_A: at lower threshold values the 'ballooning' branch is visible and stays linked to the peeling branch, as per the stability diagrams for the other discharges. However, as γ/ω_A is increased the ballooning branch rapidly recedes to lower $J_{N,ped}$ values, fully decoupling from the peeling branch at $\gamma/\omega_A = 0.06$. For the experimental point to sit on the stable side of the stability boundary, γ/ω_A needs to be at least 0.05. At this point a secondary stable region starts to appear at higher values of $J_{N,ped}$ and α, which is not seen in the other discharges. That there is a wide variation in the location of the 'ballooning' branch with γ/ω_A means that the stability boundary is not as well defined as the 'peeling' counterpart, which, combined with the intermediate mode numbers, suggests that they do not correspond to the pure high-n ideal ballooning limit but rather a mixed peeling–ballooning marginal stability limit. In fact, this is one of the key features that distinguishes the peeling–ballooning stability of MAST-U compared with its predecessor MAST (see figure 6 of [7]). For later time frames of 346 ms and 386 ms, decoupling of peeling and ballooning branches occurs for $\gamma/\omega_A \geqslant 0.05$. Given that #47018 remains ELM-free for most of this period, the experimental point should be some distance away from any stability boundaries, which further justifies the choice of $\gamma/\omega_A = 0.06$ as the threshold for this

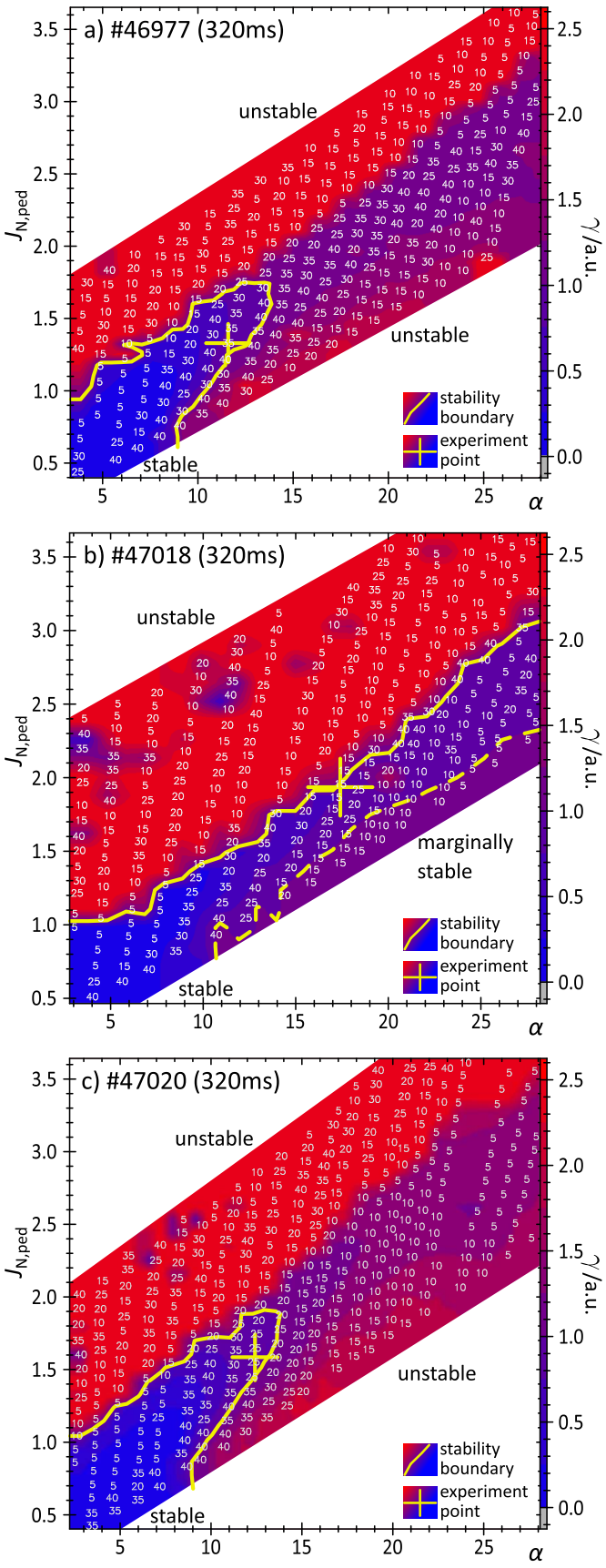

Figure 6. ELITE results for (a) #46977, (b) #47018 and (c) #47020 all at 320 ms, illustrating the locations of the stability boundary (yellow solid lines) and the distribution of the most unstable toroidal mode numbers (gray–white). The stability boundaries are defined with the growth rate threshold of $\gamma/\omega_A = 0.04$ for #46977, 0.06 for #47018 and 0.05 for #47020, which are found to be most consistent with experimental observations. The crosses indicate the locations of the experimental configurations for each case.

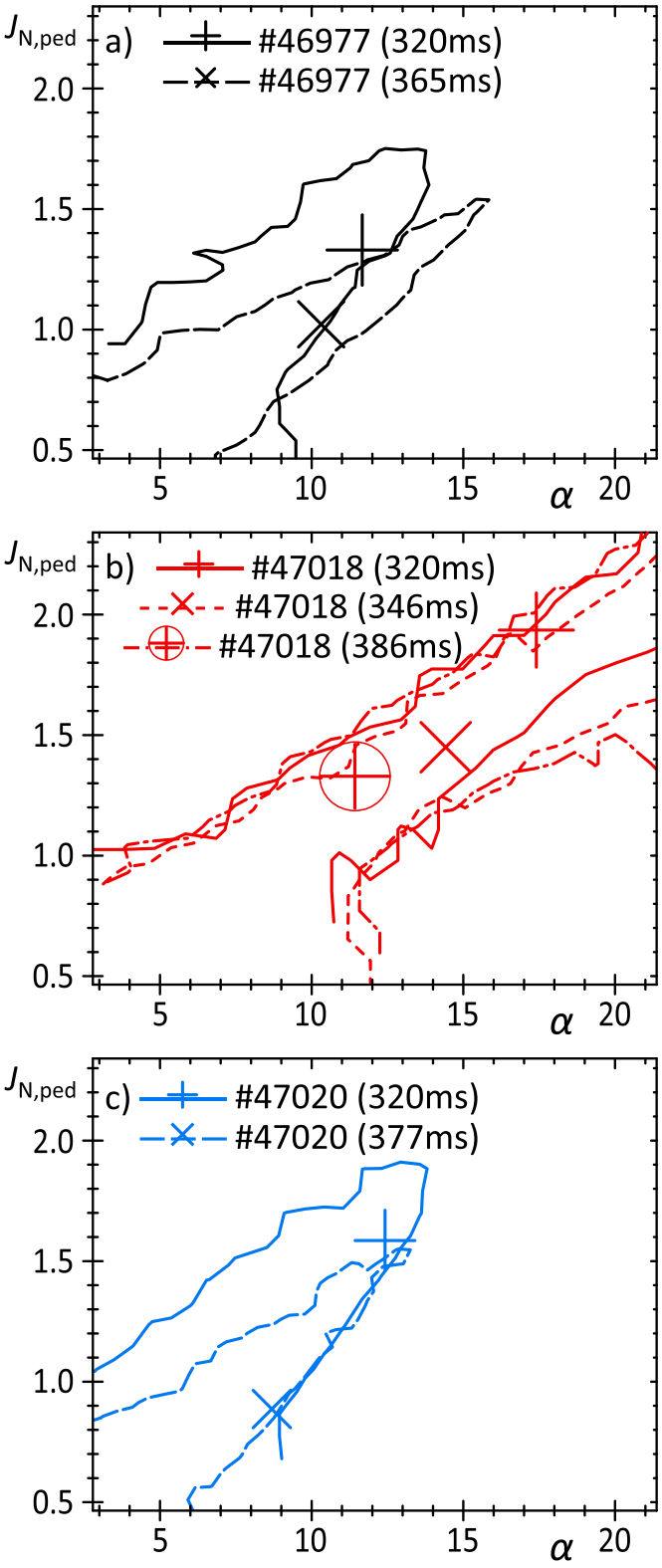

Figure 7. ELITE results illustrating the locations of the stability boundaries for (a) #46977, (b) #47018 and (c) #47020, for all analyzed time frames. The growth rate threshold for each discharge is the same as that in figure 6.

discharge. These results show that the decoupling of the stability boundary branches for #47018 is not a transient but a sustained phase, observed for the first time in MAST-U H-mode

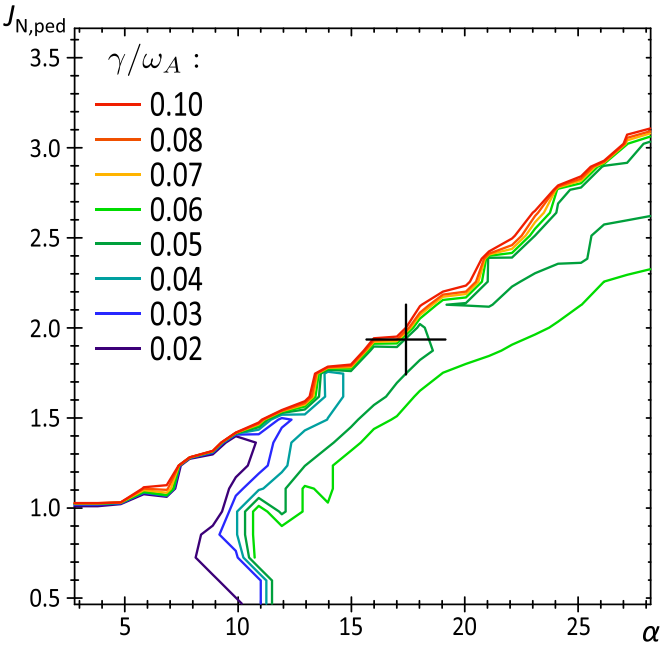

Figure 8. ELITE results for #47018 at 320 ms illustrating the variations in the locations of the stability boundary with the mode growth rate threshold relative to Alfvén frequency, γ/ω_A.

plasmas. Moreover, because of the open channel of stability, $J_{N,ped}$ and α evolve to significantly higher values, and remain higher than those of #46977 and #47020 at later times, even after a large ELM event at 365 ms.

4.2. Analysis of eigenmode structures

To further investigate the nature of different mode number distributions between the discharges, the peeling–ballooning mode eigenfunctions are calculated for #47018 and #47020 (both at 320 ms) using ELITE. The mode numbers chosen are $n = 15$ for #47018 and $n = 25$ for #47020 at the experimental points. For comparison, MAST #30422, which is an ideal ballooning-limited H-mode discharge, is also considered. Figure 9 shows the Fourier components of the radial extent of the eigenfunctions, in the pedestal region of the plasma (up to $\psi_N = 0.992$, which is the upper limit of the ELITE calculation domain in the present analysis). The case of #30422 illustrates the broader mode structure of ideal ballooning modes, with $n = 35$. On the other hand, the mode structures of #47018 and #47020 are very localized to the edge region, much like those of lower-n peeling modes, except the mode numbers here are relatively high (15 and 25, respectively). There is a subtle difference in the mode structures between the two discharges in the range $0.96 < \psi_N < 0.98$, where the slight expansion of the mode structure for #47020 is a contribution from the ballooning component.

The plots of eigenmodes as functions of the poloidal angle θ in figure 10 also show the differences in the radial mode structures between ideal ballooning-limited #30422 and the mixed peeling–ballooning-limited #47018 and #47020. In these plots, the mode structures at different radial locations

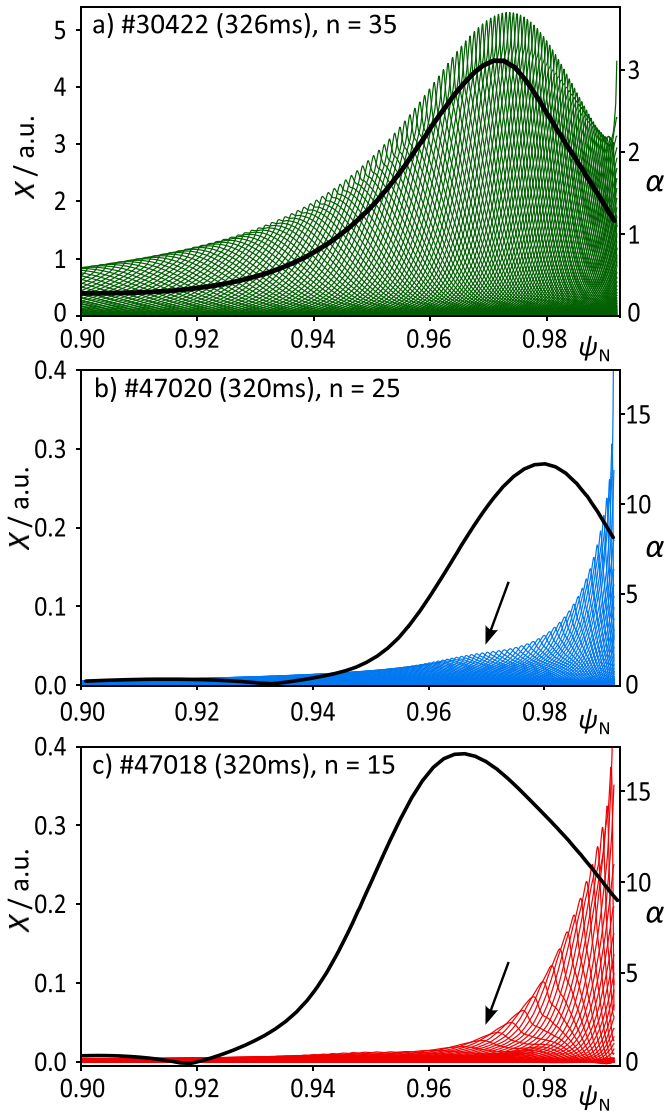

Figure 9. Fourier components of the radial extent of eigenfunctions computed by ELITE (colored lines, scale on the left), for (a) MAST #30422 (326 ms), (b) MAST-U #47020 (320 ms) and (c) MAST-U #47018 (320 ms). The black lines are the α profiles (scale on the right) over the same ψ_N range. The arrow in the #47020 plot points to the slightly extended mode structure corresponding to the ballooning component, which is absent from #47018. n on each plot is the most unstable toroidal mode number.

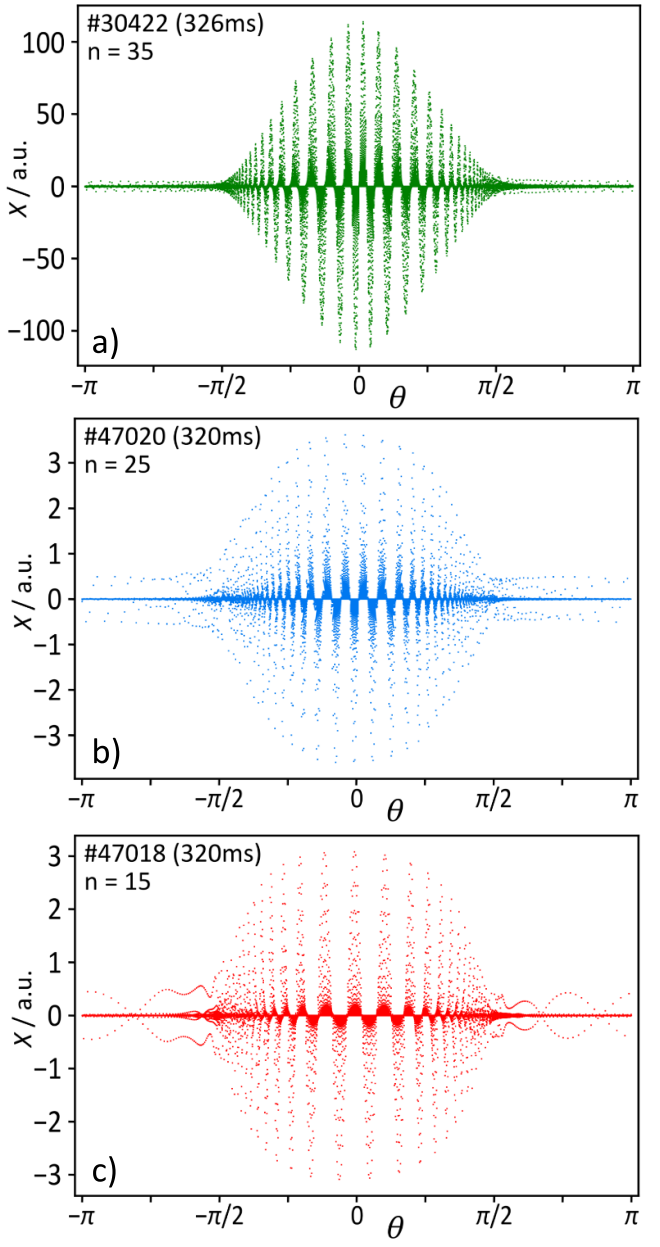

Figure 10. Plots of eigenfunctions against poloidal angle, θ, for (a) MAST #30422, (b) #47020 and (c) #47018. Mode structures at different radial locations are overlaid in each plot. $\theta = 0$ corresponds to the outer mid-plane.

are overlaid, and hence the color density provides a measure of the radial extent of the modes. For the ideal ballooning-limited #30422, the color density is higher than the other two for all amplitudes, illustrating that the radial extent of the eigenmodes is greater (as expected for ballooning-limited cases). On the other hand, for #47018 the color density is high only for lower-amplitude eigenmodes, indicating the smaller radial extent of the modes. In addition, there are some eigenmodes with a higher amplitude on the inboard side as well as around the X-points ($\theta \pm \pi/2$), both of which are a characteristic of peeling modes. The #47020 case is more intermediate, showing a greater radial extent somewhat comparable to #30422, together with higher-amplitude modes on the inboard side, similar to #47018. Nevertheless, for all three cases the mode structures are more localized to the outboard side of the plasma. It is generally found that the mode structures of MAST-U H-mode cases with an extended region of stability between the peeling and ballooning branches of the boundary, including #46977, #45270 and #45272 [7], are narrower than those of typical MAST cases, most likely because of the mixture of peeling and ballooning components present in these modes. For #47018 and #472020, the lower,

intermediate, mode numbers are likely indicative of a more dominant peeling component, although some of the characteristics of ballooning modes are still present.

5. Discussion

The peeling–ballooning stability analysis of the recent MAST-U discharges presented here shows important differences and similarities between discharge #47018 with a long ELM-free period and discharges #46977 and #47020 with steady-state type I ELMy periods. The crucial difference is in the J–α stability diagrams (figures 6 and 7), in which the decoupling of peeling and ballooning branches of the stability boundary is observed for #47018 over a sustained period of time, opening an access channel to the second stability region at higher values of $J_{\mathrm{N,ped}}$ and α, which helps to avoid the triggering of ELMs in this discharge. The significantly broader pedestal observed in #47018, along with the higher $J_{\mathrm{N,ped}}$, suggests an enhanced peeling drive compared with the other two. On the other hand, #46977 and #47020 are more comparable to other MAST-U ELMy H-mode discharges, with weakened coupling of peeling and ballooning stability boundary branches but ultimately limited by the ballooning side. However, the radial and poloidal mode structures of the three discharges are superficially similar, very localized to the narrow region near the plasma edge on the outboard side only, albeit there are differences in the most unstable mode numbers. These results suggest that these three discharges are ultimately in the mixed peeling–ballooning regime, but the differences in the early phase of the discharges have led to radically different ELM characteristics. One is in the initial evolution of the q-profile prior to L–H transition. After the current ramp-up phase, q_0 (the q-value at the magnetic axis) for #47018 decreases below 2 at a notably later time than for the other two ($\sim$280 ms for #47108, 212 ms for #47020 and 217 ms #46977), crucially long after the L–H transition period. For #46977 and #47020, the timing of q_0 hitting 2 is very close to the timing of the appearance of low-frequency MHD modes (figure 3), and also with the steep rise in pedestal temperature. It seems that the timing of the q-profile evolution, specifically the timing of the appearance of the $q = 2$ rational surface, and of the LH transition, play a crucial part in the triggering of the low-frequency MHD mode in the early phase of the discharge. Because #47018 was not plagued by this mode, the pedestal temperature was able to rise quicker than for the other two discharges, lowering the pedestal collisionality and increasing the peak in the pedestal current density. This allowed the plasma to evolve away from the ideal ballooning limit, thus avoiding type I ELMs. Further rise in the pedestal temperature and density led to significantly higher values of $J_{\mathrm{N,ped}}$ and α compared with the other discharges, until eventually the ELMs returned after 360 ms (which may have been caused by the radial shift in X-point locations from 350 ms onward).

6. Conclusion

This paper presents an analysis of the peeling–ballooning pedestal stability of the new ELM-free period observed in a MAST-U H-mode discharge. The ELM-free period in discharge #47018 coincides with a significantly higher electron pedestal temperature and lower pedestal collisionality, resulting in higher peaks in both. The stability analysis using ELITE shows that there is a decoupling of peeling and ballooning branches of the stability boundary, opening an access channel towards higher values of $J_{\mathrm{N,ped}}$ and α without triggering ELMs, which is as observed.

The mode structure analysis show that all three discharges exhibit both peeling (radial extent) and ballooning (poloidal distribution) characteristics, with no obvious distinguishing features between them (except at the most unstable mode numbers). To establish the exact nature of the mixed peeling–ballooning modes will require additional analysis incorporating non-linear effects, which is beyond the scope of the present work.

In order to fully understand the detailed mechanisms leading to the ELM-free phase of #47018, additional experimental observations are required, because although the three discharges (#46977, #47018 and #47020) had an identical setup up to 350 ms, small differences in the current ramp-up and q-profile evolution lead to significantly different ELM characteristics. For example, the connection between the evolution of q_0 and the timing of L–H transition, and consequences for the pedestal evolution and ELM characteristics, need additional experimental verification. If an MHD mode-free H-mode scenario can be reliably established, it will pave a way to accessing low-collisionality peeling-limited pedestal regimes in MAST-U, which would enable us to explore reactor-relevant, ELM-free advanced H-modes.

Data availability statement

The data cannot be made publicly available upon publication because the cost of preparing, depositing and hosting the data would be prohibitive within the terms of this research project. The data that support the findings of this study are available upon reasonable request from the authors.

Acknowledgments

This research is funded by US Department of Energy, through General Atomics (Contract Number DE-SC0018990) and

Oak Ridge National Laboratory (Contract Number DE-AC05-00OR22725), as well as UKRI Energy Programme through EPSRC, Grant Numbers EP/T012250/1 and EP/R034737/1.

Disclaimer

ORCID iDs

K Imada https://orcid.org/0000-0002-8128-2438
T H Osborne https://orcid.org/0000-0003-2641-4597
S Saarelma https://orcid.org/0000-0002-6838-2194
S Blackmore https://orcid.org/0000-0003-3754-6130
M Knolker https://orcid.org/0000-0002-8468-8767
P B Snyder https://orcid.org/0000-0002-0613-4232
C Vincent https://orcid.org/0000-0002-7227-409X
H R Wilson https://orcid.org/0000-0003-3333-7470

References

[1] Lawson J D 1957 Some criteria for a power producing thermonuclear reactor *Proc. Phys. Soc.* B **70** 6–10
[2] Wagner F *et al* 1982 Regime of improved confinement and high beta in neutral-beam-heated divertor discharges of the ASDEX tokamak *Phys. Rev. Lett.* **49** 1408–12
[3] Zohm H 1996 Edge localized modes (ELMs) *Plasma Phys. Control. Fusion* **38** 105–28
[4] Snyder P B, Wilson H R, Ferron J R, Lao L L, Leonard A W, Osborne T H, Turnbull A D, Mossessian D, Murakami M and Xu X Q 2002 Edge localized modes and the pedestal: a model based on coupled peeling–ballooning modes *Phys. Plasmas* **9** 2037–43
[5] Leonard A W 2014 Edge-localized-modes in tokamaks *Phys. Plasmas* **21** 090501
[6] Ham C J, Kirk A, Pamela S and Wilson H R 2020 Filamentary plasma eruptions and their control on the route to fusion energy *Nat. Rev. Phys.* **2** 159–67
[7] Imada K, Osborne T H, Saarelma S, Clark J G, Kirk A, Knolker M, Scannell R, Snyder P B, Vincent C and Wilson H R (the MAST Upgrade Team) 2024 Observation of a new pedestal stability regime in MAST Upgrade H-mode plasmas *Nucl. Fusion* **64** 086002
[8] Saarelma S, Hender T C, Kirk A, Meyer H, Wilson H R (the MAST Team) 2007 MHD stability analysis of ELMs in MAST *Plasma Phys. Control. Fusion* **49** 31–42
[9] Knolker M, Osborne T H, Belli E, Henderson S, Kirk A, Kogan L, Saarelma S and Snyder P B 2021 Pedestal stability analysis on MAST in preparation for MAST-U *Nucl. Fusion* **61** 046041
[10] Smith S F, Kirk A, Chapman-Oplopoiou B, Clark J G, Ham C J, Horvath L, Maggi C F, Scannell R and Saarelma S and (the MAST Team) 2022 Pedestal analysis of MAST ELMy regimes *Plasma Phys. Control. Fusion* **64** 045024
[11] Connor J W, Hastie R J, Miller R L and Wilson H R 1998 Magnetohydrodynamic stability of tokamak edge plasmas *Phys. Plasmas* **5** 2687–700
[12] Connor J W, Hastie R J and Taylor J B 1979 High mode number stability of an axisymmetric toroidal plasma *Proc. R. Soc.* A **365** 1720
[13] Wesson J A 1978 Hydrodynamic stability of tokamaks *Nucl. Fusion* **18** 87–132
[14] Snyder P B *et al* 2007 Stability and dynamics of the edge pedestal in the low collisionality regime: physics mechanisms for steady-state ELM-free operation *Nucl. Fusion* **47** 961
[15] Miller R L, Chu M S, Greene J M, Lin-Liu Y R and Waltz R E 1998 Noncircular, finite aspect ratio, local equilibrium model *Phys. Plasmas* **5** 973–8
[16] Holcomb C T *et al* 2009 Optimizing stability, transport and divertor operation in through shaping for steady-state scenario development in DIII-D *Phys. Plasmas* **16** 056116
[17] Wilson H R and Miller R L 1999 Access to second stability region for coupled peeling–ballooning modes in tokamaks *Phys. Plasmas* **6** 873–6
[18] Burrell K H *et al* 2001 Quiescent double barrier high-confinement mode plasmas in the DIII-D tokamak *Phys. Plasmas* **8** 2153–62
[19] Whyte D G *et al* 2010 I-mode: an H-mode energy confinement regime with L-mode particle transport in Alcator C-Mod *Nucl. Fusion* **50** 105005
[20] Menghini O and Lao L L 2013 Integrated modeling of tokamak experiments with OMFIT *Plasma Fusion Res.* **8** 2403009
[21] Menghini O *et al* 2015 Integrated modeling applications for tokamak experiments with OMFIT *Nucl. Fusion* **55** 083008
[22] Lao L L, John H S Stambaugh R D, Kellman A G and Pfeiffer W 1985 Reconstruction of current profile parameters and plasma shapes in tokamaks *Nucl. Fusion* **25** 1611–22
[23] Hawryluk R J 1981 An empirical approach to tokamak transport *Phys. Plasmas Close Thermonuclear Cond.* **1** 19–46
[24] Grierson B A *et al* 2018 Orchestrating TRANSP simulations for interpretative and predictive tokamak modeling with OMFIT *Fusion Sci. Technol.* **74** 101–15
[25] Kogan L *et al* (the MAST-Uteam) 2022 First MAST-U equilibrium reconstructions using the EFIT++ code *48th EPS Conf. on Plasma Physics* p 2a.116
[26] Snyder P B *et al* 2009 Pedestal stability comparison and ITER pedestal prediction *Nucl. Fusion* **49** 085035
[27] Osborne T H *et al* 2015 Enhanced H-mode pedestals with lithium injection in DIII-D *Nucl. Fusion* **55** 063018
[28] Wilson H R, Snyder P B, Huysmans G T A and Miller R L 2002 Numerical studies of edge localized instabilities in tokamaks *Phys. Plasmas* **9** 1277–12886
[29] Snape J A, Gibson K J, O'Gorman T, Barratt N C, Imada K, Wilson H R, Tallents G J and Chapman I T and the MAST Team 2012 The influence of finite radial transport on the structure and evolution of $m/n = 2/1$ neoclassical tearing

modes on MAST *Plasma Phys. Control. Fusion* **54** 085001
[30] La Haye R J, Buttery R J, Gerhardt S P, Sabbagh S A and Brennan D P 2012 Aspect ratio effects on neoclassical tearing modes from comparison between DIII-D and national spherical torus experiment *Phys. Plasmas* **19** 062506
[31] Sauter O, Angioni C and Lin-Liu Y R 1999 Neoclassical conductivity and bootstrap current formulas for general axisymmetric equilibria and arbitrary collisionality regime *Phys. Plasmas* **6** 2834–9
[32] Sauter O, Angioni C and Lin-Liu Y R 2002 Erratum: Neoclassical conductivity and bootstrap current formulas for general axisymmetric equilibria and arbitrary collisionality regime *Phys. Plasmas* **9** 5140
[33] Knolker M *et al* 2018 Investigation of the role of pedestal pressure and collisionality on type-I ELM divertor heat loads in DIII-D *Nucl. Fusion* **58** 096023